


Local discrimination of orbital angular momentum in entangled states

Simone Cialdi, Edoardo Suerra^{✉,*}, Samuele Altiglia, Stefano Olivares, Bruno Paroli,
 Marco A. C. Potenza[✉], Mirko Siano[✉], and Matteo G. A. Paris
Università degli Studi di Milano and Istituto Nazionale di Fisica Nucleare, Milan, Italy

 (Received 29 September 2023; revised 28 December 2023; accepted 16 September 2024; published 1 October 2024)

In this paper, we address the use of a calcite crystal-based local detector for the discrimination of the orbital angular momentum of quantum radiation produced by parametric down-conversion, using only a portion of the beam. Specifically, we propose and experimentally demonstrate that discrimination can be achieved by exploiting the introduction of a precise and controlled spatial shift between two replicas of the state within the crystals. This approach utilizes a robust and intrinsically stable monolithic configuration, obviating the need for feedback mechanisms or thermal drift compensation. Our method offers a promising avenue for enhancing the reliability and efficiency of quantum communication systems, and we believe that this technology could significantly advance the development of quantum communication techniques, where information encoding is based on orbital angular momentum, or spatially distributed orbital angular momentum detection.

DOI: [10.1103/PhysRevA.110.043701](https://doi.org/10.1103/PhysRevA.110.043701)

I. INTRODUCTION

Radiation with orbital angular momentum (OAM) [1] has given rise to many applications to overcome the diffraction limit in imaging methods [2], in astronomical and astrophysical observations [3,4], to finely control and manipulate nanoparticles [5], detection of the gravitational waves [6], and in the field of telecommunications [7–9]. OAM beams exhibit twisting helical wavefronts with a phase singularity at the center. The helical wavefronts are characterized by an integer number l , known as the topological charge, which describes the number of 2π phase shifts around the optical axis. The topological charge is also associated to the quantized orbital angular momentum $l\hbar$ of a single photon [10]. In particular over the past years, considerable attention has been paid to the conservation of orbital angular momentum in spontaneous parametric down-conversion (SPDC) [10–13] which finds potential applications in experimental quantum information science. The detection of OAM states is of utmost importance for the full exploitation of OAM-based systems. To this aim, different interferometric [14–16], diffractive [17], and refractive [18,19] techniques have been proposed, leading to efficient sorters of OAM states [20,21] capable of fast (single-shot) performances [22]. Notwithstanding the availability of accurate and well-established OAM detection techniques, even current state-of-the-art methods require collecting a substantial portion or the entire wavefront of the OAM beam, and in many cases the singularity should also be intercepted by the detector surface. In some applications, the OAM beam can become larger than the detector size due to the natural photon beam divergence, particularly for higher topological charges l , posing serious limitations to OAM states decoding. In this view, we have recently investigated and experimentally

proven the possibility of measuring the topological charge, thus of detecting OAM states, by using only a small portion of the propagating beam [23–27]. In this paper, we propose and experimentally demonstrate an effective approach to detect OAM entangled states generated by SPDC with a monolithic interferometer based on two birefringent crystals. As such, the proposed scheme is intrinsically stable and does not require any feedback or thermal drift compensation.

II. THE BASIC IDEA

In general, a Laguerre-Gauss (LG) mode $\psi_{p,l}(x, y)$ depends on a radial index p and an angular index l . Here, we set $p = 0$, since this corresponds to our actual experimental configuration, as we will discuss below, so that the (non-normalized) LG mode can be written as

$$\psi_{0,l}(x, y) = e^{-r^2/w^2} r^{|l|} e^{-il\phi}, \quad (1)$$

where $r = \sqrt{x^2 + y^2}$ and $\phi = \text{atan2}(y, x)$, (x, y) are the Cartesian coordinates, and w is the beam waist. Note atan2 is the two-argument arctangent. Notice that we neglect the Guoy phase for the reasons explained below. The helical phase front of the mode is exploited in the proposed technique to discriminate between OAM states. Basically, the LG mode is sent through a suitable interferometer, where it is split into two different paths that experience different longitudinal phase shifts, thus acquiring a relative phase shift φ . The two paths are then superimposed with an additional transverse shift, here only along the y axis for simplicity, of an amount Δy , so that the complex amplitude of the total radiation leaving the interferometer is given by

$$\psi_{0,l}^{(\text{out})}(x, y; \Delta y) = \psi_{0,l}(x, y) + \psi_{0,l}(x, y - \Delta y)e^{i\varphi}.$$

Notice that in the operational conditions of our application, the Rayleigh range of the input beam is much larger than the beams' separation in the interferometer. Consequently, the

*Contact author: edoardo.suerra@unimi.it

Guoy phase of the two beams is essentially the same, and when they interfere it serves as a common factor that does not impact the intensity pattern. For this reason, we neglect it in Eq. (1). If the amplitude $\psi_{0,l}^{(\text{out})}(x, y)$ is associated with a single photon, as in the case we are going to consider, then the probability of detecting it at a given point, say for simplicity $(x_0, 0)$, is

$$P(\varphi, l) = |\psi_l^{(\text{out})}(x_0, y; \Delta y)|^2 = \xi^2 + 2\alpha\beta \cos(\varphi + l\phi_0), \quad (2)$$

where $\phi_0 = \arctan(\Delta y, x_0)$, $\alpha = \exp(-x_0^2/w^2)|x_0|^{l/2}$, $\beta = \exp[-(x_0^2 + \Delta y^2)/w^2](x_0^2 + \Delta y^2)^{l/2}$, and $\xi^2 = \alpha^2 + \beta^2$. Equation (2) shows that interference fringes form with a phase shift $l\phi_0$, so properly measuring $P(\varphi, l)$ allows retrieving information about the angular index l , which is the idea behind the local detection of OAM with our technique.

III. THEORY

In this section, we calculate the states generated via SPDC in terms of LG modes, and we resume the main elements necessary to describe the local discrimination of OAM states.

Let us focus on a SPDC in collinear configuration. The state generated in this condition can be written as [28]

$$|\psi\rangle_{\text{PDC}} = \int d^2\mathbf{r} A_{\text{pump}}(\mathbf{r}) a_1^\dagger(\mathbf{r}) a_2^\dagger(\mathbf{r}) |0\rangle, \quad (3)$$

where $\mathbf{r} = (x, y)$, $A_{\text{pump}}(\mathbf{r})$ is the complex amplitude of the pump in the spatial domain, and $a_{1,2}^\dagger(\mathbf{r}) = \int d^2\mathbf{k} \exp(-i\mathbf{k} \cdot \mathbf{r}) a_{1,2}^\dagger(\mathbf{k})$ are the creation operators of the photon at the point \mathbf{r} , with $\mathbf{k} = (k_x, k_y)$. Introducing the single-mode state

$$|\psi_{\text{LG}}\rangle_{p,l} = \int d^2\mathbf{r} \psi_{p,l}(\mathbf{r}) a^\dagger(\mathbf{r}) |0\rangle,$$

where $\psi_{p,l}$ are the LG modes with radial index p and angular index l , and by means of the completeness relation $\sum_{p,l} |\psi_{\text{LG}}\rangle_{p,l} \langle\psi_{\text{LG}}| = 1$, Eq. (3) becomes

$$|\psi\rangle_{\text{PDC}} = \sum_{p,l} \sum_{p',l'} c_{p,l,p',l'} |\psi_{\text{LG}}\rangle_{p,l} |\psi_{\text{LG}}\rangle_{p',l'},$$

where $c_{p,l,p',l'} = \int d^2\mathbf{r} A_{\text{pump}}(\mathbf{r}) \psi_{p,l}^*(\mathbf{r}) \psi_{p',l'}^*(\mathbf{r})$. Since for postselection we only detect states with $p = p' = 0$, we focus on the coefficients $c_{l,l'} := c_{0,l,0,l'}$. For a Gaussian laser pump profile $A_{\text{pump}}(\mathbf{r}) \propto \exp(-r^2/w_p^2)$ with a waist w_p , as in our case, the equation for OAM conservation holds,

$$c_{l,l'} \propto \int r dr e^{-\frac{r^2}{w_p^2}} e^{-\frac{r^2}{w_p^2}} r^{|l|+|l'|} \int d\phi e^{i(l+l')\phi}, \quad (4)$$

which vanishes for $l + l' \neq 0$. Defining $|l\rangle = |\psi_{\text{LG}}\rangle_{0,l} = \int d^2\mathbf{r} \psi_l(\mathbf{r}) a^\dagger(\mathbf{r}) |0\rangle$, we clearly see that our PDC state is entangled in OAM:

$$|\psi\rangle_{\text{PDC}} = \sum_l c_{l,-l} |l\rangle_1 |-l\rangle_2. \quad (5)$$

After the two entangled photons of the state of Eq. (5) are separated, for example, by using a beam splitter, the detection of the modes with different OAM l can be performed locally as described above.

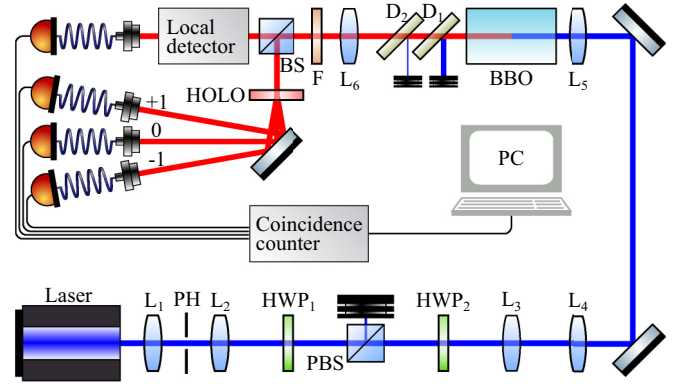


FIG. 1. Scheme of the experimental setup. Laser: laser diode; L_i : lenses; PH: pinhole; HWP_i : half-wave plates; BBO: BBO crystal; D_i : dichroic mirrors; F: long-pass filter; BS: beam splitter; HOLO: hologram; 0, ± 1 : OAM modes separated by the hologram.

IV. EXPERIMENTAL IMPLEMENTATION

The idea for OAM detection described in the section above has been experimentally implemented and demonstrated using the setup depicted in Fig. 1. Pump radiation is provided by a 407.5-nm wavelength laser diode, spatially filtered with the lenses L_1 and L_2 in a confocal configuration, together with a pinhole (PH) placed in their common focal point. Power adjustment is performed with an amplitude modulator formed by a half-wave plate (HWP_1) and a polarizing beam splitter (PBS). Another half-wave plate (HWP_2) sets the right polarization for the SPDC process. A telescopic system L_3 and L_4 , and the lens L_5 guarantee a size of the spot in the SPDC crystal of $40\ \mu\text{m}$. Type-I SPDC is obtained by means of a 1-mm-long beta barium borate (BBO) crystal. Two dichroic mirrors D_1 and D_2 , together with a long-pass filter F_1 , remove the residual pump radiation. Collimation of the PDC photons is achieved using the lens L_6 with a focal length 100 mm, then a 50 : 50 beam splitter (BS) separates the two entangled photons, making their separation effective only in 50% of cases. The reflection of BS goes to a computer-generated fork hologram made on a polyester film with groove density of ≈ 30 lines/mm, that separates $l = 0$, $l = 1$, and $l = -1$ modes, which are successively sent to three corresponding single-mode fiber couplers, each connected to different avalanche photodiodes. This specific hologram limits the application of our technique only to the modes with $l = \pm 1$, but other hologram configurations could be used in order to study different OAMs, for example, generated by non-null pump OAM. Furthermore, fiber couplers automatically define the modes' dimension of the other entangled photon, since they transmit only collimated photons in the mode LG_{00} , and with a diameter of 2.38 mm. The transmission of BS goes to the local detector, described in the next section, where another in-fiber avalanche photodiode allows photon counting. An *ad hoc* electronic device and a computer (PC) allow the simultaneous coincidence photon counts between the output of the interferometer and the $l = \pm 1$ outputs of the hologram. Notice that, due to OAM conservation, a coincidence with the $l = \pm 1$ output of the holograms implies that a $l = \mp 1$ state exits the interferometer.

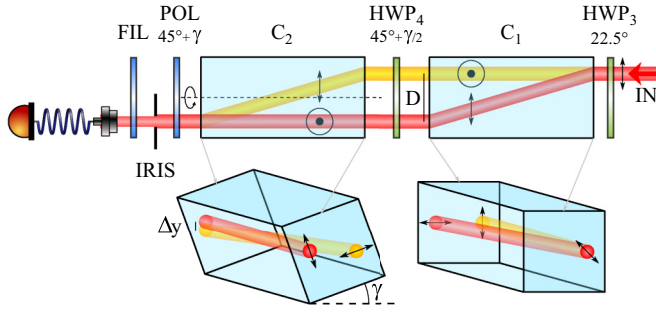


FIG. 2. Scheme of the local detector from above. IN: input beam; HWP_i : half-wave plates; C_i : calcite crystals; POL: polarizer; IRIS: iris; FIL: spectral filter. The effect of C_2 rotation around the sketched axis is clear in the three-dimensional (3D) view, consisting in a vertical separation Δy of the two replica of the beam.

Detection of OAM states is performed with a local detector, which exploits the principle described at the end of the theoretical section [see Eq. (2)]. This detector is based on two identical 40-mm-long calcite crystals, schematized in Fig. 2. The input polarization of the photons from PDC is horizontal, and it is rotated to 45° with a half-wave plate (HWP_3). The first calcite crystal C_1 is oriented in a direction such that vertical and horizontal polarizations encounter ordinary and extraordinary paths, respectively. In this last case, the walk-off is $D = 4.18$ mm at the end of the crystal. Another half-wave plate (HWP_4) rotates the polarization of each path such that they result inverted in the second calcite crystal C_2 . After passing through C_2 , the two paths intersect and allows interference, which can be seen after a 45° polarizer (POL). Finally, an iris (IRIS), and a 10-nm-FWHM spectral filter (FIL) perform a spatial and spectral selection, respectively. Looking at Eq. (2), the phase shift φ between the two paths is set by slightly rotating C_1 around the vertical axis by means of a stepper motor connected to the crystal mount, and controlled by a computer. The other parameter Δy is controlled by rotating C_2 around the longitudinal axis, as schematized in Fig. 2. More specifically, rotating C_2 of a small angle γ causes the overlap of parts of the mode that were shifted of $\Delta y = D \sin \gamma \approx D \gamma$. A horizontal shift occurs too, but it is negligible, since $\Delta x = D(1 - \cos \gamma) \approx 0$. The presence of the iris makes the detection local, since its aperture is always smaller than the beam size. In our case, the minimum diameter of the iris has been chosen in order to have a reasonable coincidence photon counts rate (in our case $\approx 500 \text{ min}^{-1}$), and corresponds to 1.5 mm, so that only a fraction of the beam power is collected (in our case from 45% to 30%, corresponding to iris horizontal shifts from 0 to 0.8 mm, respectively). Measuring coincidences between hologram outputs and interferometer output for different φ allows the reconstruction of the probability $P(\varphi, \pm 1)$, and thus the synchronous detection of $l = \pm 1$ states. A final brief examination should be devoted to the impact of the finite radius of curvature R of the input beam. Specifically, this curvature induces interference fringes in the vertical direction (aligned with the shift introduced by the interferometer), thereby diminishing visibility. The requisite condition for preventing this effect is expressed as $R \gg d_i \Delta y / \lambda$, with d_i the iris diameter. Notice that in the

following calculations we included the effect of a finite value of R , to ensure a complete analysis. Owing to its design, this interferometer results to be very robust and stable, both for the shift Δy and the phase shift φ , providing a very important tool, especially for long-term measurements, as in our case.

V. NUMERICAL CALCULATIONS AND EXPERIMENTAL RESULTS

Our experimental setup allows the measurement of coincidence counts relative to the OAM $l = +1$ and $l = -1$, thus in this section, we will show the expected results relative to these cases, in particular as a function of the vertical shift Δy , the iris dimension, and the iris horizontal shift x_0 , together with the experimental results. Before delving into the calculations, it is important to highlight the effects of the angular correlations between the entangled photons, and the mode divergence. As far as the angular correlations are concerned, the projection onto an LG mode can be non-null also for non-perfectly-collinear modes. For example, let us consider the LG_{00} mode. The position of the coupler 0, after the hologram, fixes the dimensions of the mode coupled to the calcite crystal, since only an LG_{00} with a diameter of 2.38 mm enters the fiber and can be detected. Actually, the hologram does not transform an LG_{01} into an ideal LG_{00} , and, in turn, it results in coupling a mode generated from a LG_{01} with a dimension $w = 0.85$ mm. Propagating back to the BBO crystal, this corresponds to a $31 \mu\text{m}$ beam. The coupler 0 also fixes the direction of the photon on the BS reflection, thus the direction of the entangled photon on the BS transmission has an angular spectrum that depends on the pump dimensions. Equation (4) becomes for LG_{00} modes

$$c_{0,0}(\theta) = \int r dr d\phi e^{-\frac{r^2}{w_p^2} - \frac{2r^2}{w^2}} e^{i\frac{2\pi}{\lambda} \theta r \cos \phi} \propto e^{-\frac{\tilde{w}^2}{4} k^2},$$

where $k = 2\pi\theta/\lambda$, and $\tilde{w}^{-2} = w_p^{-2} + 2w^{-2}$. Here, θ is the exit angle of the photon propagating to the local detector with respect to the condition of perfect collinearity, while w_p is the pump beam radius ($40 \mu\text{m}$), and w is the radius of the beam collected by the fiber couplers ($31 \mu\text{m}$). In these conditions, the angular spectrum $\delta_{\text{PDC}} = \lambda/\pi\tilde{w}$ is comparable to the diffraction of the same mode $\delta_{\text{diff}} = \lambda/\pi w$, thus the effect is non-negligible, and it must be considered by incoherently summing the contributions relative to all the angular spectra, weighted on the corresponding amplitudes. The same holds for LG_{01} modes, and we have

$$c_{1,-1}(\theta) = \int r dr d\phi e^{-\frac{r^2}{w_p^2} - \frac{2r^2}{w^2}} \left(\frac{\sqrt{2}r}{w_s} \right)^2 e^{i\frac{2\pi}{\lambda} \theta r \cos \phi}.$$

Since the angular deviation is converted into a shift by the collimation lens L_6 , δ_{PDC} is converted into a transverse shift by $L_6 \delta_{\text{PDC}}$. The aforementioned incoherent sum is performed over all the incoherent contributions relative to different translations both on x and y directions, with a Gaussian weight $G(r) = \exp(-2r^2/w_c^2)$, where $w_c = 0.93$ mm is the shift corresponding to δ_{PDC} . It is crucial to note that this effect highlights the importance of using the collimating lens L_6 , since, without it, paths with different θ would experience different shifts in the interferometer, leading to a significant

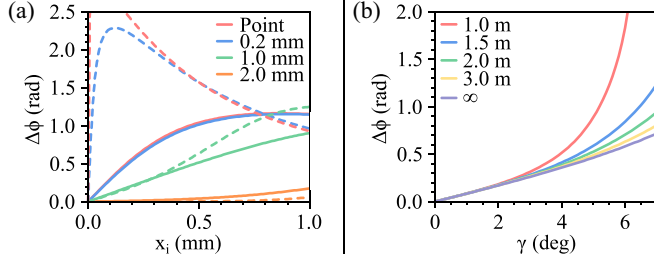


FIG. 3. (a) Calculation of the shift $\Delta\phi$ as a function of the horizontal position of the iris x_i , with (solid) and without (dashed) considering the angular correlations between the entangled photons, for different iris diameters d_i . Here, $\Delta y = 0.5$ mm, corresponding to $\gamma \approx 7^\circ$. (b) Calculation of the shift $\Delta\phi$ as a function of the rotation γ of the crystal C_2 , for different beam radii of curvature. Here, $x_i = 0.7$ mm and $y_i = 0$.

reduction in fringe visibility. The other aforementioned effect concerns the divergence of the beams, that is important due to the small dimensions of the beams we use. In particular, we observed that radii of curvature shorter than 3 m lead to vertical fringes in the interferometer, resulting in a decreased visibility due to the vertical shift. On the other hand, this effect can also lead to an increase in the phase shift between the two paths in the interferometer, as will be clear from the calculations below. Notice that the reduction in visibility may differ between the $l = +1$ and $l = -1$ beams, since their radii of curvature are generally not exactly equal.

Figure 3(a) shows the calculations of the phase shift $\Delta\phi$ between the probabilities $P(\varphi, l)$ of $l = +1$ and $l = -1$ as a function of the horizontal shift x_0 of the iris, and for different iris diameters [$d_i = 0$ (point), 0.2, 1.0, and 2.0 mm]. In these calculations, we set $\Delta y = 0.5$ mm, corresponding to $\gamma \approx 7^\circ$. We considered the cases with and without angular correlations, corresponding to solid and dashed lines, respectively. It is clear that the total effect of the angular correlations is to reduce $\Delta\phi$, even if it remains relevant for our purpose. Notice that the curves tend to the point case as the iris aperture decreases, as one would expect. In Fig. 3(b) we report the phase shift between $l = +1$ and $l = -1$ cases as a function of the rotation γ of the crystal C_2 , for different radii of curvature of the two beams. The position of the iris in this case is $x_i = 0.7$ mm and $y_i = 0$. We notice that the phase shift increases as the radius of curvature decreases.

Exploiting the setup described above, we simultaneously measured coincidence photon counts between the output of the interferometer and the $l = \pm 1$ outputs of the hologram, as a function of φ , and in different configurations. Precisely, for each value of φ , coincidence counts have been sent to a PC, allowing the reconstruction of the probabilities $P(\varphi, \pm 1)$, as reported in Fig. 4, left columns (points). Every experimental point is the average of 25 acquisitions, each of 40 s. Each data set has been fitted with the function $y = A + B \cos(\varphi + C)$ (lines), from which the respective phase shifts $\Delta\phi$ have been calculated, and it is reported in the right column of Fig. 4 (blue points), together with the theoretical trends (lines), calculated for different radii of curvature. After verifying that

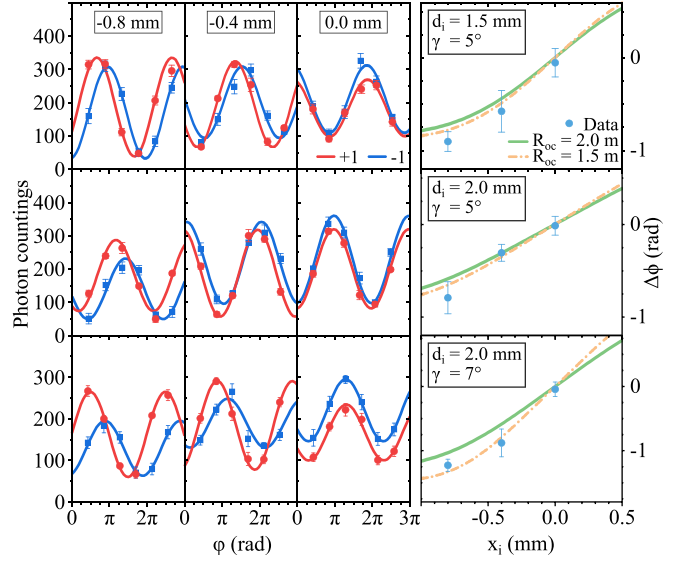


FIG. 4. On the left, we show the acquired sinusoids of Eq. (2) for different iris positions x_i (-0.8 , -0.4 , and 0.0 mm), with their respective fits. The resulting shift $\Delta\phi$ is plotted in the corresponding graphs on the right, comparing the results with theoretical trends (lines). Each row corresponds to different iris diameters d_i and crystal rotation angles γ .

$\Delta\phi$ is null for $\Delta y = 0$, we acquired data for different iris positions x_i , iris diameters d_i , and rotation angles γ of the crystal C_2 . The comparison between experimental points and theoretical trends shows that the method is robust and fits well with a radius of curvature of the beams of around 1.5 m. This confirms that our approach is really local, in the sense explained above, and our technique can be effectively used to distinguish between different OAMs. Owing to the local nature of the measurement, this technique could be used also for the discrimination of spatially distributed OAMs.

VI. CONCLUSIONS

In this paper, we have demonstrated the use of a monolithic interferometer utilizing two birefringent calcite crystals to effectively discriminate the topological charge of quantum radiation carrying orbital angular momentum. This interferometer is intrinsically stable and does not require any feedback or thermal drift compensation. Our experimental setup, which employs a two-photon entangled state generated by spontaneous parametric down-conversion, has confirmed the efficacy of the proposed method, showing strong agreement with theoretical predictions. As the interferometer requires only a portion of the beam to be detected, it ensures local discrimination of the OAM of entangled states.

ACKNOWLEDGMENT

This work was supported by the National Institute for Nuclear Physics (INFN) (project: ADAMANT).

- [1] L. Allen, M. Beijersbergen, R. Spreeuw, and J. Woerdman, Orbital angular momentum of light and the transformation of Laguerre–Gaussian laser modes, *Phys. Rev. A* **45**, 8185 (1992).
- [2] F. Tamburini, G. Anzolin, G. Umbriaco, A. Bianchini, and C. Barbieri, Overcoming the Rayleigh criterion limit with optical vortices, *Phys. Rev. Lett.* **97**, 163903 (2006).
- [3] F. Tamburini, B. Thidé, G. Molina-Terriza, and G. Anzolin, Twisting of light around rotating black holes, *Nat. Phys.* **7**, 195 (2011).
- [4] G. C. G. Berkhout and M. W. Beijersbergen, Method for probing the orbital angular momentum of optical vortices in electromagnetic waves from astronomical objects, *Phys. Rev. Lett.* **101**, 100801 (2008).
- [5] Y. Ma, G. Rui, B. Gu, and Y. Cui, Trapping and manipulation of nanoparticles using multifocal optical vortex metalens, *Sci. Rep.* **7**, 14611 (2017).
- [6] B. Mours, E. Tournefier, and J. Vinet, Thermal noise reduction in interferometric gravitational wave antennas: Using high order TEM modes, *Class. Quantum Grav.* **23**, 5777 (2006).
- [7] Y. Yan, G. Xie, M. Lavery, H. Huang, N. Ahmed, C. Bao, Y. Ren, Y. Cao, L. Li, Z. Zhao, A. Molisch, M. Tur, M. Padgett, and A. Willner, High-capacity millimetre-wave communications with orbital angular momentum multiplexing, *Nat. Commun.* **5**, 4876 (2014).
- [8] M. Krenn, R. Fickler, M. Fink, J. Handsteiner, M. Malik, T. Scheidl, R. Ursin, and A. Zeilinger, Communication with spatially modulated light through turbulent air across Vienna, *New J. Phys.* **16**, 113028 (2014).
- [9] G. Xie, Y. Ren, Y. Yan, H. Huang, N. Ahmed, L. Li, Z. Zhao, C. Bao, M. Tur, S. Ashrafi, and A. Willner, Experimental demonstration of a 200-Gbit/s free-space optical link by multiplexing Laguerre–Gaussian beams with different radial indices, *Opt. Lett.* **41**, 3447 (2016).
- [10] A. Mair, A. Vaziri, G. Weihs, and A. Zeilinger, Entanglement of the orbital angular momentum states of photons, *Nature (London)* **412**, 313 (2001).
- [11] S. Franke-Arnold, S. Barnett, M. Padgett, and L. Allen, Two-photon entanglement of orbital angular momentum states, *Phys. Rev. A* **65**, 033823 (2002).
- [12] G. Barbosa, Transverse coincidence structures in spontaneous parametric down-conversion with orbital angular momentum: Theory, *Phys. Rev. A* **76**, 033821 (2007).
- [13] S. Feng and P. Kumar, Spatial symmetry and conservation of orbital angular momentum in spontaneous parametric down-conversion, *Phys. Rev. Lett.* **101**, 163602 (2008).
- [14] J. Vickers, M. Burch, R. Vyas, and S. Singh, Phase and interference properties of optical vortex beams, *J. Opt. Soc. Am. A* **25**, 823 (2008).
- [15] Y. Shen, G. Campbell, B. Hage, H. Zou, B. Buchler, and P. Lam, Generation and interferometric analysis of high charge optical vortices, *J. Opt.* **15**, 044005 (2013).
- [16] H. Zhou, S. Yan, J. Dong, and X. Zhang, Double metal subwavelength slit arrays interference to measure the orbital angular momentum and the polarization of light, *Opt. Lett.* **39**, 3173 (2014).
- [17] G. Ruffato, M. Massari, G. Parisi, and F. Romanato, Test of mode-division multiplexing and demultiplexing in free-space with diffractive transformation optics, *Opt. Express* **25**, 7859 (2017).
- [18] M. Lavery, D. Robertson, G. Berkhout, G. Love, M. Padgett, and J. Courtial, Refractive elements for the measurement of the orbital angular momentum of a single photon, *Opt. Express* **20**, 2110 (2012).
- [19] C. Li and S. Zhao, Efficient separating orbital angular momentum mode with radial varying phase, *Photonics Res.* **5**, 267 (2017).
- [20] G. Berkhout, M. Lavery, J. Courtial, M. Beijersbergen, and M. Padgett, Efficient sorting of orbital angular momentum states of light, *Phys. Rev. Lett.* **105**, 153601 (2010).
- [21] M. Mirhosseini, M. Malik, Z. Shi, and R. Boyd, Efficient separation of the orbital angular momentum eigenstates of light, *Nat. Commun.* **4**, 2781 (2013).
- [22] G. Kulkarni, R. Sahu, O. Magaña-Loaiza, R. Boyd, and A. Jha, Single-shot measurement of the orbital-angular-momentum spectrum of light, *Nat. Commun.* **8**, 1054 (2017).
- [23] B. Paroli, M. Siano, and M. Potenza, Dense-code free space transmission by local demultiplexing optical states of a composed vortex, *Opt. Express* **29**, 14412 (2021).
- [24] B. Paroli, M. Siano, and M. Potenza, Measuring the topological charge of orbital angular momentum radiation in single-shot by means of the wavefront intrinsic curvature, *Appl. Opt.* **59**, 5258 (2020).
- [25] B. Paroli, M. Siano, and M. Potenza, A composite beam of radiation with orbital angular momentum allows effective local, single-shot measurement of topological charge, *Opt. Commun.* **459**, 125049 (2020).
- [26] B. Paroli, L. Cremonesi, M. Siano, and M. Potenza, Hybrid OAM-amplitude multiplexing and demultiplexing of incoherent optical states, *Opt. Commun.* **524**, 128808 (2022).
- [27] M. Siano, B. Paroli, S. Cialdi, S. Olivares, M. Paris, E. Suerra, and M. Potenza, Experimental high sensitive local identification of azimuthal index of Laguerre–Gauss beams, *Opt. Commun.* **557**, 130349 (2024).
- [28] F. Miatto, A. Yao, and S. Barnett, Full characterization of the quantum spiral bandwidth of entangled biphotons, *Phys. Rev. A* **83**, 033816 (2011).